Supplementary Information (SI) for Journal of Materials Chemistry A.

Supporting Information

High-Performance Supercapacitor Electrode Based on Zn/V Co-Doped $NiMoO_4$: A Cation–Cation Doping Strategy

Fatemeh Kazemi Kerdabadi [a], Parviz Kameli [a*], Mohamad Mohsen Momeni [b*], Tapati Sarkar [d], Bagher Aslibeiki [c,d]

[a] *Department of Physics, Isfahan University of Technology, Isfahan, 84156-83111, Iran*

[b] *Department of Chemistry, Isfahan University of Technology, Isfahan, 84156-83111, Iran*

[c] *Department of Physics, University of Tabriz, Tabriz, Iran*

[d] *Department of Materials Science and Engineering, Uppsala University, Box 35, Uppsala SE-75103, Sweden*

1. Material Characterization

---

[*] Corresponding authors.
E-mail addresses: kameli@iut.ac.ir (P. Kameli), mm.momeni@iut.ac.ir (M.M. Momeni).

X-ray diffraction patterns were recorded using a Siemens D5000 diffractometer to study the crystalline structure of the samples. Raman spectra were collected using a Horiba Jobin-Yvon Labram HR800 with excitation wavelength of 532 nm to confirm the functional bonding and groups. A Zeiss LEO 1550 scanning electron microcopy equipped with energy-dispersive X-ray spectroscopy was employed to study the morphology of the samples. X-ray photoelectron spectrum (XPS) was recorded to analyze the elemental composition and valence state by employing a PHI QUANTERA II X-ray photoelectron spectrometer (XPS) with Al K-alpha source. To investigate the optical properties and bandgap, UV-Vis spectroscopy was measured in the wavelength range of 190–1100 nm using a Lambda 25 Perkin Elmer spectrophotometer.

2. Electrochemical Properties and Performance Evaluation

The electrochemical performance of the synthesized samples was systematically investigated using a three-electrode configuration in an aqueous medium. Commercial nickel foam substrates (dimensions: 1 cm × 5 cm) were pretreated by ultrasonic immersion in 3 M HCl, followed by sequential rinsing with ethanol and deionized (DI) water. This cleaning protocol effectively activated the surface and removed residual contaminants and native oxide layers. The six doped nanorod slurry-coated on pre-treated NF served as working electrodes, while a platinum wire and an Ag/AgCl electrode were employed as the counter and reference electrodes, respectively. To prepare the working electrode, a slurry was formulated by mixing 80 wt% of the active material, 10 wt% acetylene carbon black, and 10 wt% polyvinylidene fluoride (PVDF) binder, dissolved in N-methyl-2-pyrrolidone (NMP). This mixture was uniformly coated onto a nickel substrate (1×2 cm^2), with an active area of 1×1 cm^2 containing approximately 1–1.4 mg of material. The coated electrodes were dried at 70 °C for 2 h to minimize residual impurities. The cross-sectional FE-SEM analysis revealed an average active layer thickness of 7.5 µm, obtaining the electrode volume within the active region was approximately 0.00075 cm^3, with an effective porosity of 71.1%. Electrochemical measurements were performed in 3 mol L^{-1} KOH aqueous electrolyte using an IVIUM electrochemical workstation within a potential range of 0 to 0.8 V. Electrochemical impedance spectroscopy (EIS) was conducted over a frequency range of 0.01 Hz to 1 MHz at a bias voltage of 0.2 V in the fully charged state. The internal resistance (iR) drop was calculated by subtracting the discharge voltage drop, obtained from the GCD plots, from the total voltage. To ensure statistical relevance and reproducibility, measurements were repeated on at least three independently prepared electrodes for each composition.

The fundamental formula for calculating the porosity of materials is according to the following relationships:

$$\epsilon = 1 - \frac{\text{Bulk Density } (\rho_{\text{bulk}})}{\text{Theoretical Density } (\rho_{\text{theo}})} \tag{S1}$$

$$\epsilon = 1 - \frac{m_{\text{total}} / \rho_{\text{theoretical}}}{\text{Volume}_{\text{ electrode}}} \tag{S2}$$

Where ρ_{bulk} is the bulk density, ρ_{theo} is the theoretical density, and ϵ indicates porosity of the material.

Table S1: Quantitative metrics of the prepared electrodes, including mass loading, geometrical dimensions, porosity, and surface area.

Required Metric	Value	Measurement Method
Mass Loading per Area	1 to 1.4 mg cm^{-2}	Direct weighting
Electrode Thickness	7.5 µm	Cross-section FE-SEM
Electrode volume	0.00075 cm^3	-
Porosity	59.5% to 71.1%	*
$a_{s,BET}$	518.7 m^2 g^{-1}	BET analysis

3. Williamson–Hall (W–H) method

The Williamson–Hall (W–H) method was employed to analyze the XRD peak broadening, enabling the simultaneous estimation of crystallite size and lattice strain. This approach distinguishes the contributions of size-induced and strain-induced effects, providing deeper insight into the structural properties of the material [1].

$$\beta\cos\theta = \frac{K\lambda}{D} + 4\varepsilon\, sin\theta \qquad \text{(S3)}$$

where K is the constant, λ is the wavelength of X-ray radiation, β is the full width half maximum (FWHM) of a diffraction peak expressed in radians, and θ is the diffraction angle.

Table S2: Lattice strain and crystallite-particle size obtained from Williamson−Hall equation (S1).

Sample	Strain (ε)	Crystallite Size (D, nm)
NM	0.0024	103
Z-NM	0.0028	62
V-NM	0.0031	45
ZV-NM3	0.0051	28

4. Calculating atomic concentration (at%.) of the sample

To quantify the elemental composition, the atomic percentages were calculated using the corrected peak areas and corresponding sensitivity factors in XPS analysis according to the following equation [2,3].

$$C_i = \frac{(A_i/S_i)}{\sum_j (A_j/S_j)} \times 100\% \qquad \text{(S4)}$$

Where A_i is the peak area, S_i is the sensitivity factor for element i and C_i indicates atomic percentage of element *i*.

Table S3: Sensitivity-factor corrected atomic percentages of $NiMoO_4$ and doped samples.

	Atomic percentage $C_i\%$				
sample	**Ni**	**Mo**	**O**	**Zn**	**V**
$NiMoO_4$ (NM)	22.41	22.59	55.55	-	-
Zn doped NM (Z-NM)	14.25	21.8	59.94	4.01	-
V doped NM (V-NM)	19.3	19.49	59.35	-	1.86
Zn/V doped NM (ZV-NM3)	17.44	18.67	61.12	1.01	1.78

5. Asymmetric Supercapacitors (ASC):

4.1. Fabrication and Performance Evaluation of the ZV-NM3-Based Asymmetric Supercapacitor:

To assess the practical viability of the synthesized ZV-NM3/NF electrode for energy storage applications, a pouch-type asymmetric supercapacitor (ASC) device was constructed. The device configuration consisted of two electrodes separated by a Whatman filter paper, which served as a physical barrier to prevent direct contact while allowing ion migration through the electrolyte. The ZV-NM3 composite served as the positive electrode, and a commercial graphite sheet (GS, 99% purity) was employed as the negative electrode. The graphite sheet had a thickness of 0.19 mm, a mass of 0.063 g for a 2×2 cm² (4 cm²) electrode area, corresponding to an areal loading of 15.75 mg cm^{-2}. Both electrodes were immersed in a PVA/KOH gel electrolyte, which acted as the ion-conductive medium. The gel electrolyte was prepared by dissolving 1.5 g of polyvinyl alcohol (PVA) in 15 mL of deionized water under continuous stirring at room temperature. After achieving full dissolution, 2.5 mL of 3 M KOH solution was gradually added to 5 mL of the prepared PVA solution while stirring, yielding a transparent gel suitable for ion transport. The

ZV-NM3 electrode, integrated with graphite sheet, was optimized to operate across a wide potential window of 1.8 V, which defines the working range of the ASC device. The mass ratio between the negative and positive electrodes was calculated based on charge balance principles [1-2], using the following equations:

$$\frac{m^{+}}{m^{-}} = \frac{C^{-} \times \Delta V^{-}}{C^{+} \times \Delta V^{+}} \tag{S5}$$

where m^+ and m^- are the mass loadings of positive (ZV-NM3) and graphite sheet current collectors. C^+ and C^- stand for the specific capacitance of the positive and negative electrodes, and ΔV^+ and ΔV^- represent the potential window of positive and negative electrodes, respectively. The aqueous-based electrolytes are used to minimize the cost of the materials, especially for the electrolyte. Asymmetric supercapacitors are explored using an aqueous electrolyte, in which EDLC carbon-based materials can be used as the negative electrode, while Faradaic transition metal oxide/hydroxide/sulfide materials can be used as positive electrode materials. The higher operational potential window, high energy density and high-power density could be possible to achieve in ASCs. The formula for calculating the specific capacitance (Cs, Fg^{-1}), energy density (E, Wh kg^{-1}), and power density (P, W kg^{-1}) of the ASC device is given below as Equations (S3)–(S6):

$$Csp = \frac{1}{m\mu\Delta v}\int_{a}^{b} ivdv \tag{S6}$$

$$C_s = \frac{I \times \Delta t}{m \times \Delta V} \quad (Fg^{-1}) \tag{S7}$$

$$E = \frac{c_s \times (\Delta V)^2}{2 \times 3.6}(\ Wh\ kg^{-1}) \tag{S8}$$

$$P = \frac{E \times 3600}{\Delta t}(\ W\ kg^{-1}) \tag{S9}$$

where “I” is the discharge current (A), “m” is the weight of the active material, “µ” is the scan rate (V s^{-1}), “Δt” is the discharge time (sec), and “ΔV” is the potential window (V). Notably, the performance of the solid-state device was normalized to the total active mass of both electrodes.

Notably, for non-linear GCD profiles, the quasi-reversible faradaic reactions result in asymmetric charge–discharge curves. In such cases, the charge-to-voltage ratio of the faradaic process is no longer constant but varies over time. Therefore, the specific capacitance for non-linear GCD curves was determined using the following equation [6].

$$C = \frac{2i_m \int Vdt}{V^2 \Big|_{Vi}^{Vf}} \qquad \text{(S10)}$$

Here, the i_m= I/m (A g^{-1}) is the current density, where I is the current and m is the active mass of the electrode. $\int Vdt$ is the galvanostatic discharge current area, where V is the potential with initial and final values of V_i and V_f, respectively.

The voltammetric charge (Q^*) was calculated using the following equation [4,5]:

$$Q^* = \frac{Area\ under\ the\ CV\ curve}{Area\ of\ the\ electrode\ \left(cm^2\right) \times Scan\ rate\ (\frac{mV}{s}} \qquad \text{(S11)}$$

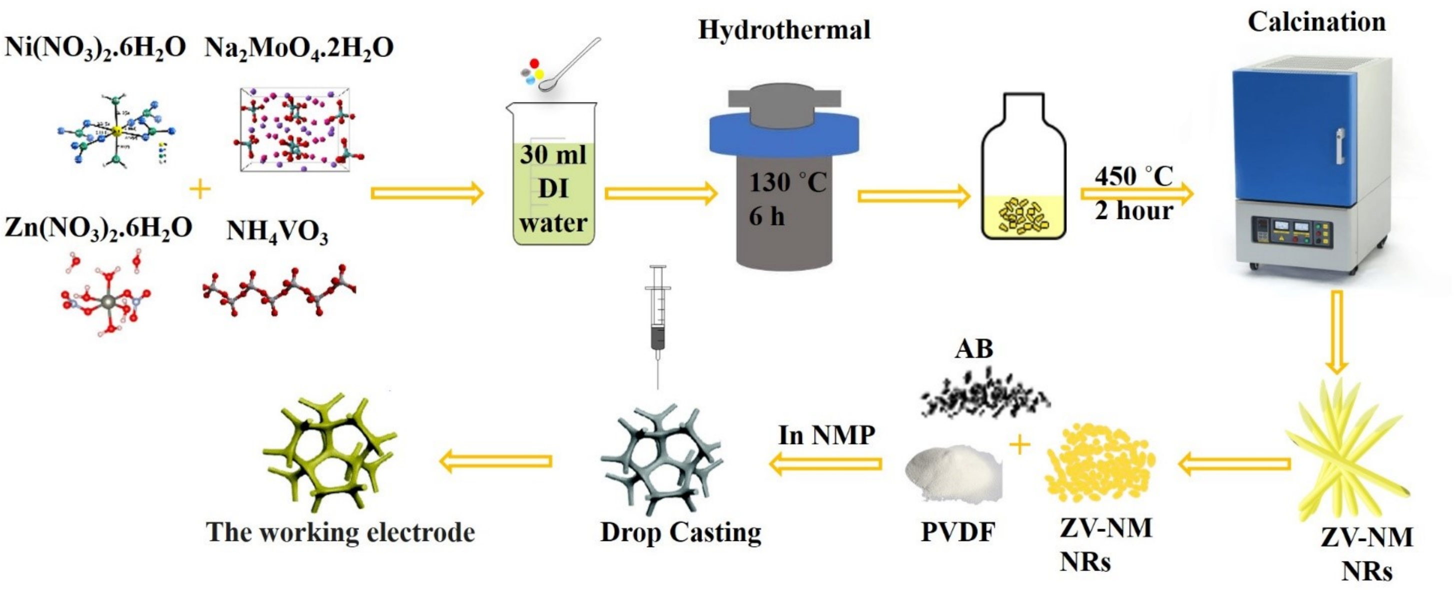

Figure S1: Schematic of the synthesis and preparation of Zn/V dual-doped $NiMoO_4$ nanorod electrode.

Table S4: Amount of precursors used for the synthesis of different electrode materials.

	Amount of starting materials			
sample	$Na_2MoO_4.2H_2O$ (mmol)	$Ni(NO_3)_2.6H_2O$ (mmol)	$Zn(NO_3)_2.6H_2O$ (x mmol)	NH_4VO_3 (y mmol)
$NiMoO_4$ (NM)	1	1	-	-
Zn doped NM (Z-NM)	1	0.75	0.25	-
V doped NM (V-NM)	1	0.75	-	0.25
Zn/V doped NM (ZV-NM1)	1	0.75	0.125	0.125
Zn/V doped NM (ZV-NM2)	1	0.75	0.1875	0.0625
Zn/V doped NM (ZV-NM3)	1	0.75	0.0625	0.1875

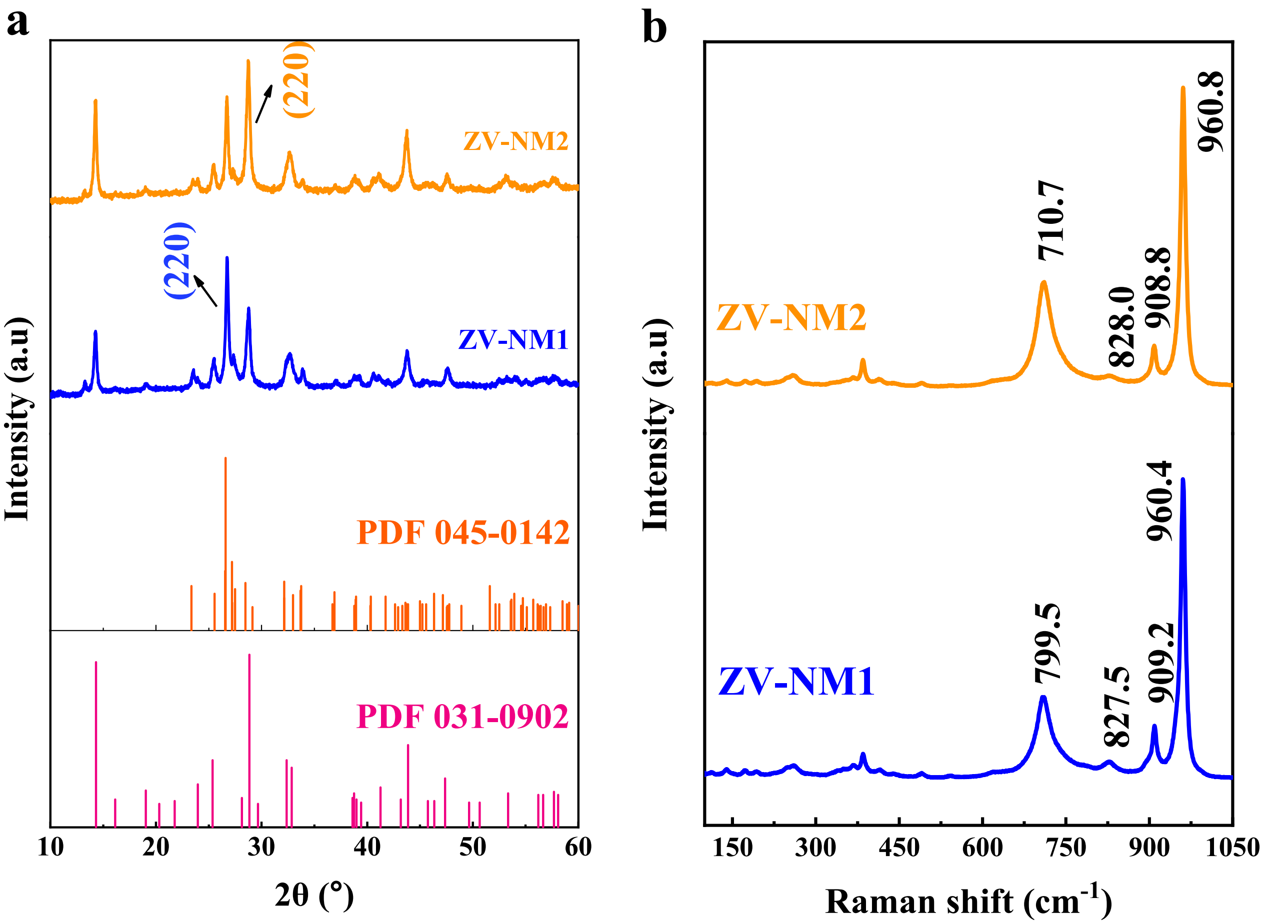

Figure S2: (a) XRD, and (b) Raman spectra for the ZV-NM1 and ZV-NM2 electrodes.

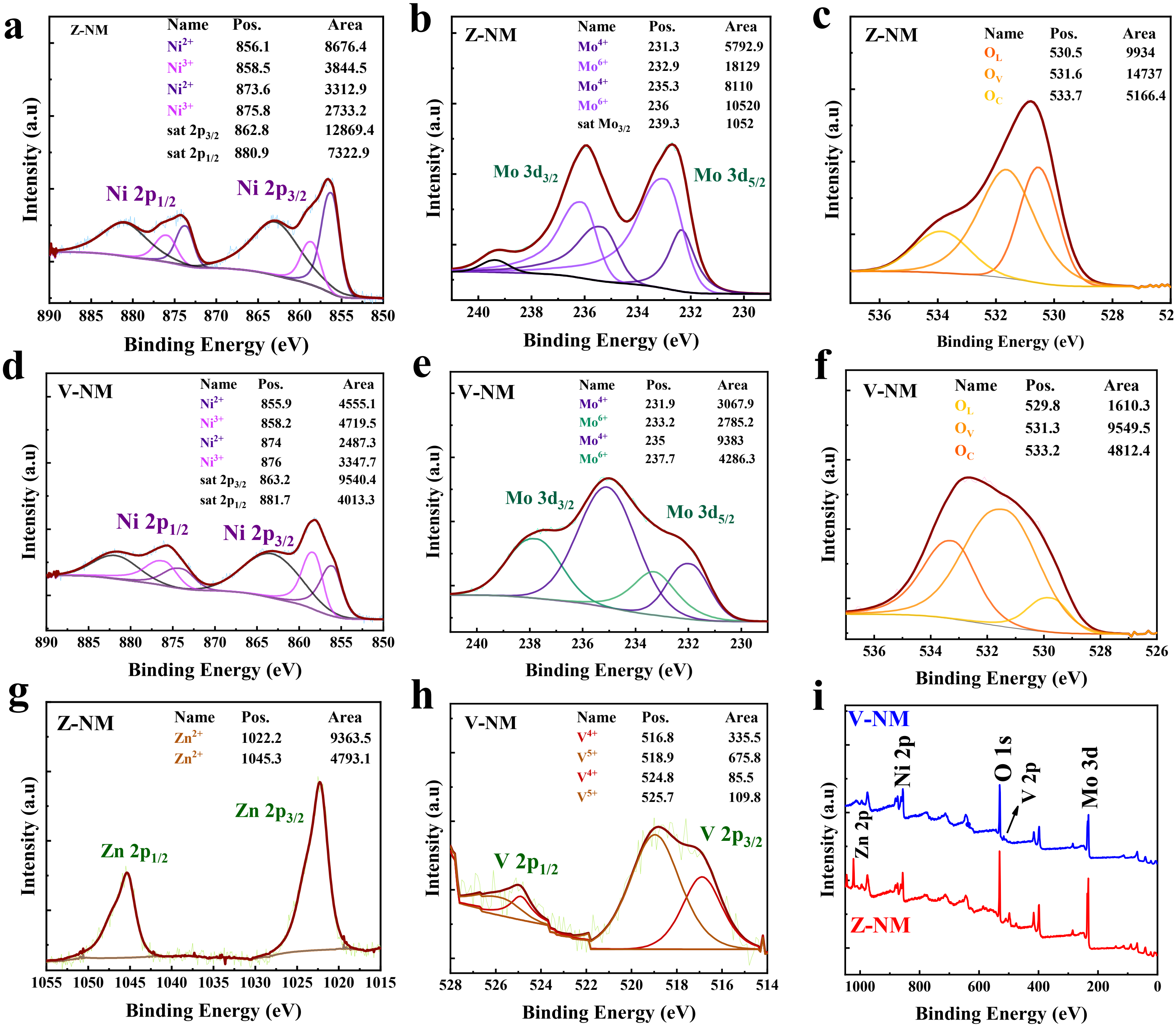

Name	Pos.	Area
Ni^{2+}	856.1	8676.4
Ni^{3+}	858.5	3844.5
Ni^{2+}	873.6	3312.9
Ni^{3+}	875.8	2733.2
sat $2p_{3/2}$	862.8	12869.4
sat $2p_{1/2}$	880.9	7322.9

Name	Pos.	Area
Mo^{4+}	231.3	5792.9
Mo^{6+}	232.9	18129
Mo^{4+}	235.3	8110
Mo^{6+}	236	10520
sat $Mo_{3/2}$	239.3	1052

Name	Pos.	Area
O_L	530.5	9934
O_V	531.6	14737
O_C	533.7	5166.4

Name	Pos.	Area
Ni^{2+}	855.9	4555.1
Ni^{3+}	858.2	4719.5
Ni^{2+}	874	2487.3
Ni^{3+}	876	3347.7
sat $2p_{3/2}$	863.2	9540.4
sat $2p_{1/2}$	881.7	4013.3

Name	Pos.	Area
Mo^{4+}	231.9	3067.9
Mo^{6+}	233.2	2785.2
Mo^{4+}	235	9383
Mo^{6+}	237.7	4286.3

Name	Pos.	Area
O_L	529.8	1610.3
O_V	531.3	9549.5
O_C	533.2	4812.4

Name	Pos.	Area
Zn^{2+}	1022.2	9363.5
Zn^{2+}	1045.3	4793.1

Name	Pos.	Area
V^{4+}	516.8	335.5
V^{5+}	518.9	675.8
V^{4+}	524.8	85.5
V^{5+}	525.7	109.8

Figure S3: (a-f) High-resolution XPS spectra for Ni 2p, Mo 3d, and O 1s, (g-h) The spectra of Zn 2p and V 2p, and (i) A comparative survey spectra of Z-NM and the V-NM samples.

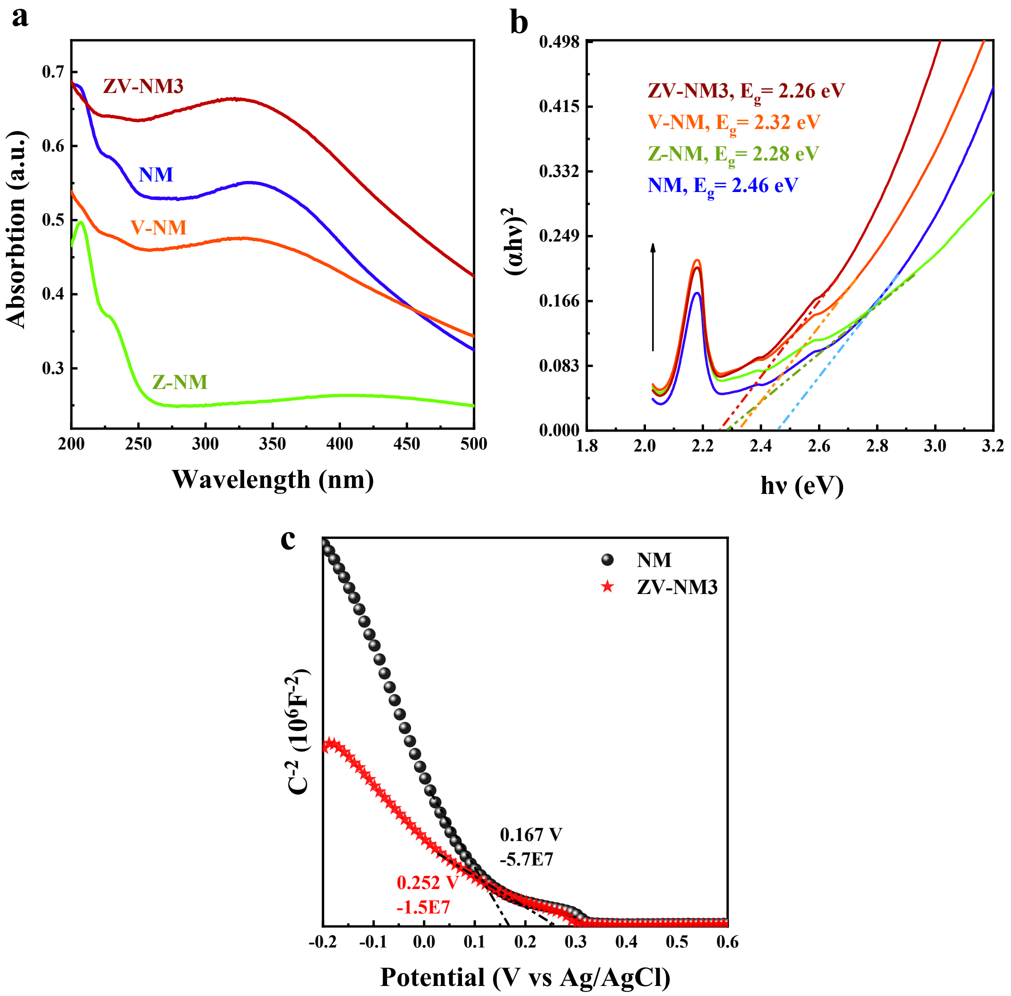

Figure S4: (a) UV-Vis spectra, (b) Tauc plot for the direct band gap of all four $NiMoO_4$-based nanorods, and (c) Mott-Schottky plot of NM and ZV-NM3 electrode.

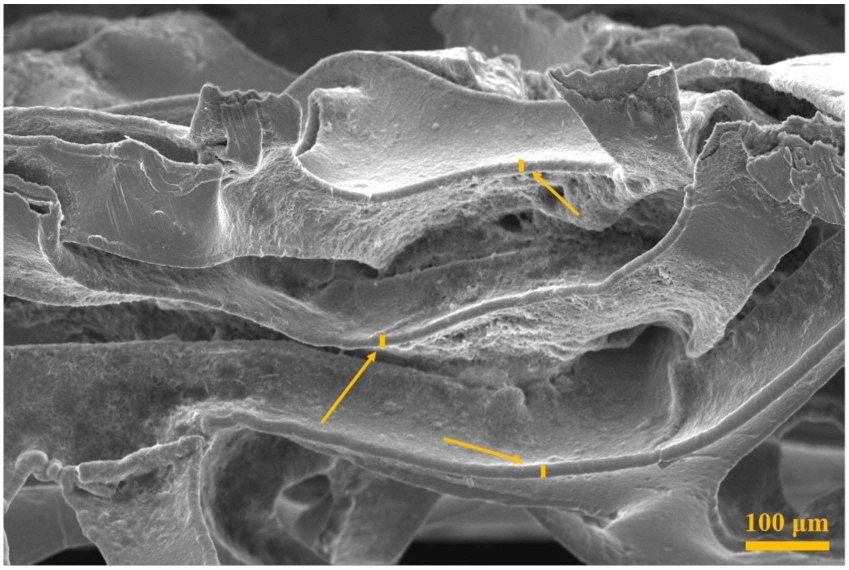

Figure S5: Cross-sectional FESEM image of ZV-NM3/NF electrode.

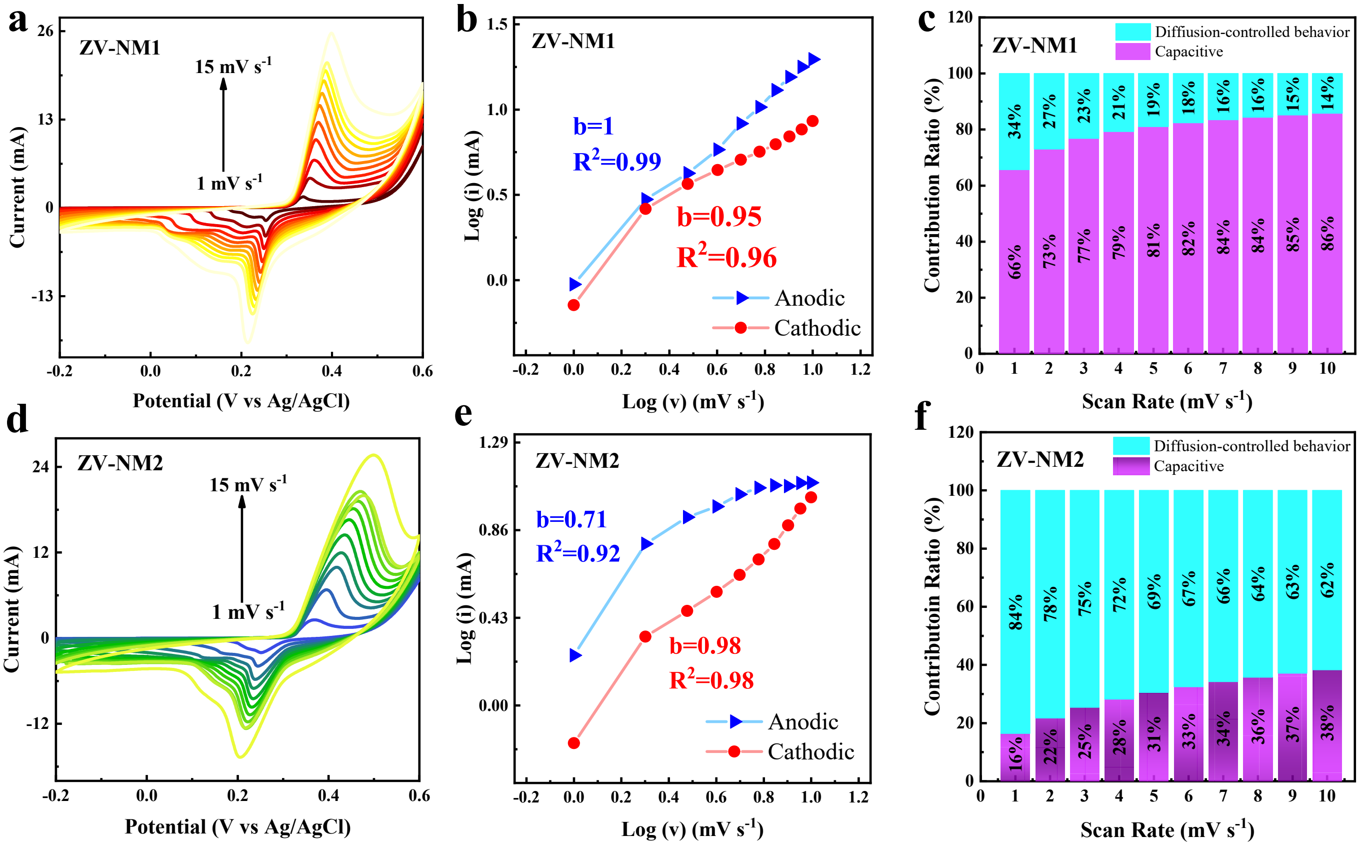

Figure S6: (a-c) CV curve at different scan rates, log(υ) vs. log (i) profile for finding the b-value, and percentage contribution of surface capacitance and diffusion-controlled capacitance for the ZV-NM1/NF, and (d-f) for the ZV-NM2/NF electrodes.

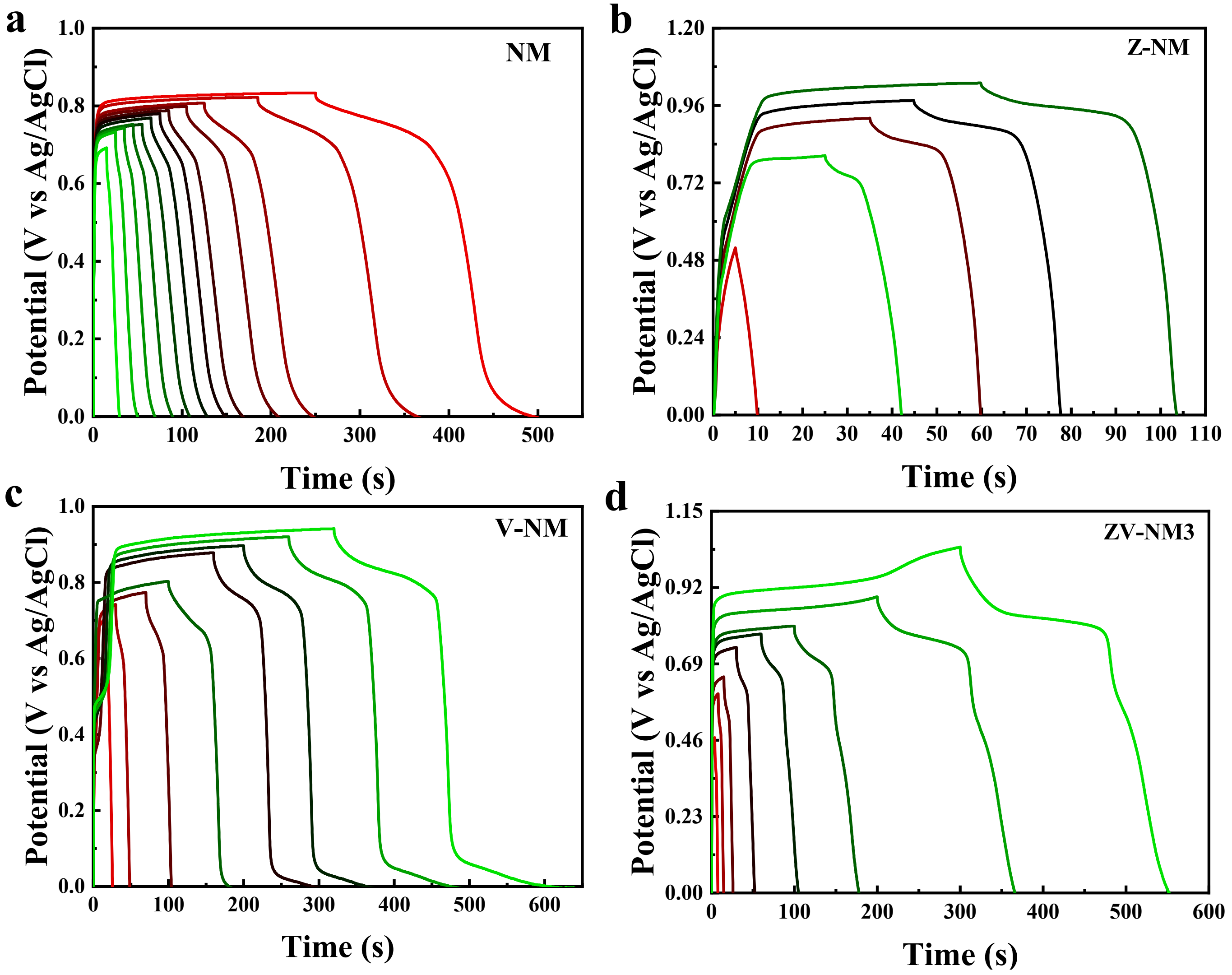

Figure S7: GCD curves at various potentials ranging from 0.5 to 1 V with a current density of 0.5 mA cm^{-2} for (a) NM/NF, (b) Z-NM/NF, (c) V-NM/NF, and (d) ZV-NM3/NF electrodes in a three-electrode system.

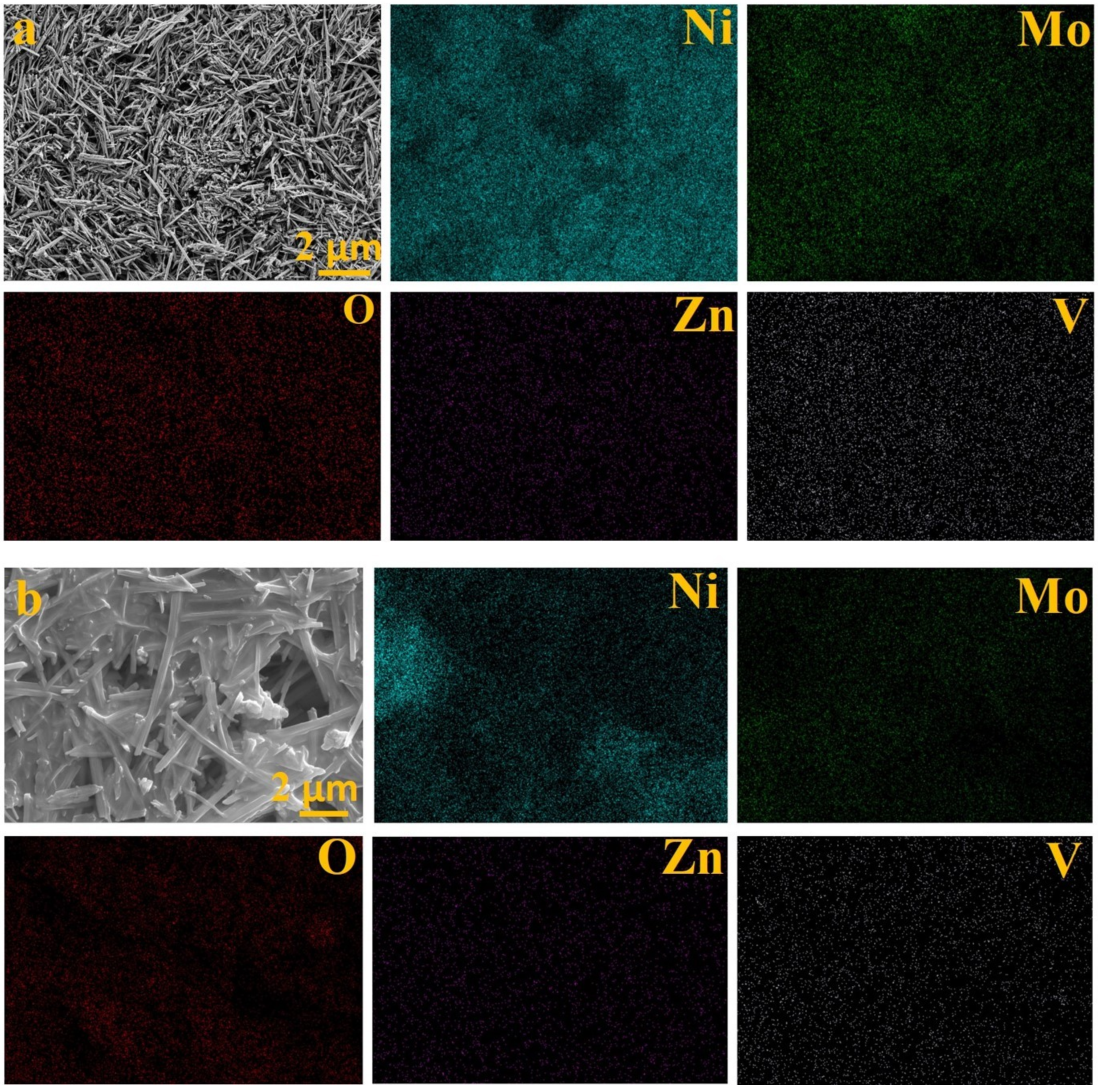

Figure S8: (a) FE-SEM and EDX elemental mapping of the ZV-NM3 electrode before, and (b) after 10000th cycling.

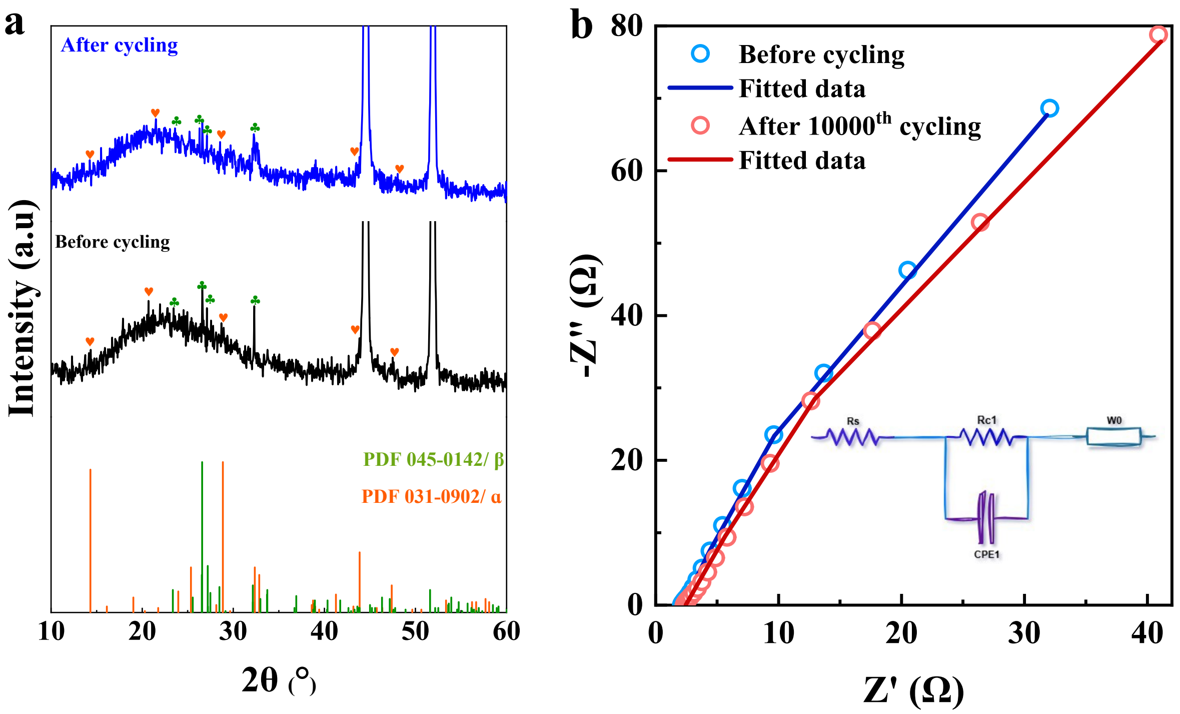

Figure S9: (a) XRD profile, and (b) EIS curves of before and after 10000th cycling of ZV-NM3 electrode.

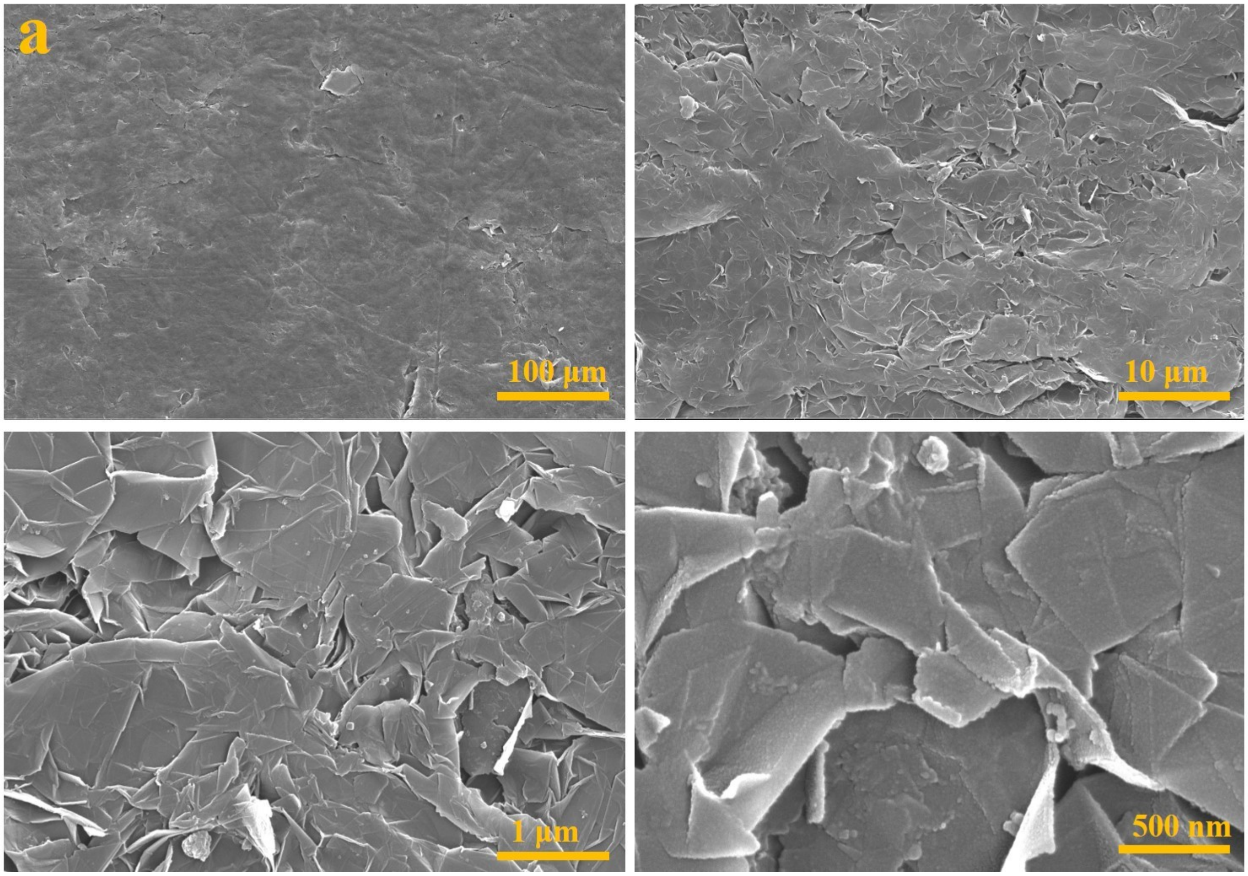

Figure S10: (a) FE-SEM micrographs of the negative electrode (GS) at different magnifications.

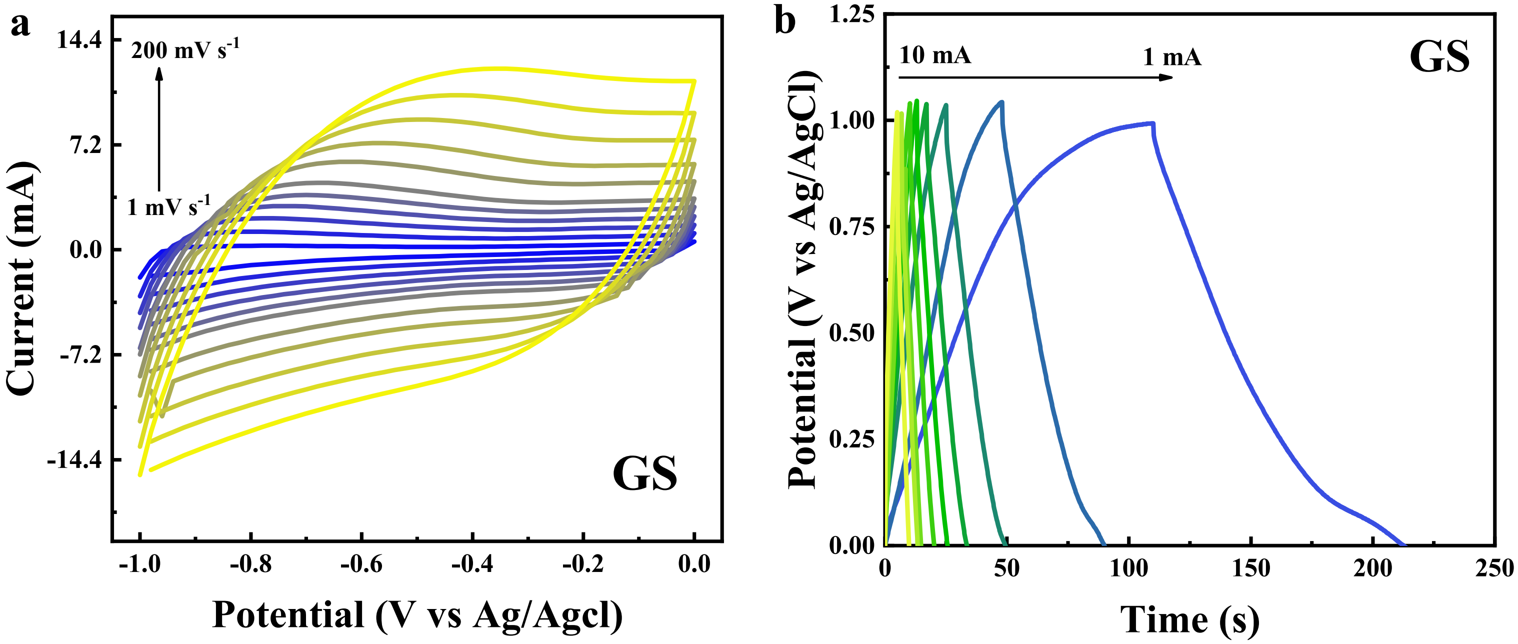

Figure S11: (a) CV curve at different scan rates, and (b) GCD profiles of graphite sheet (GS) at various current densities.

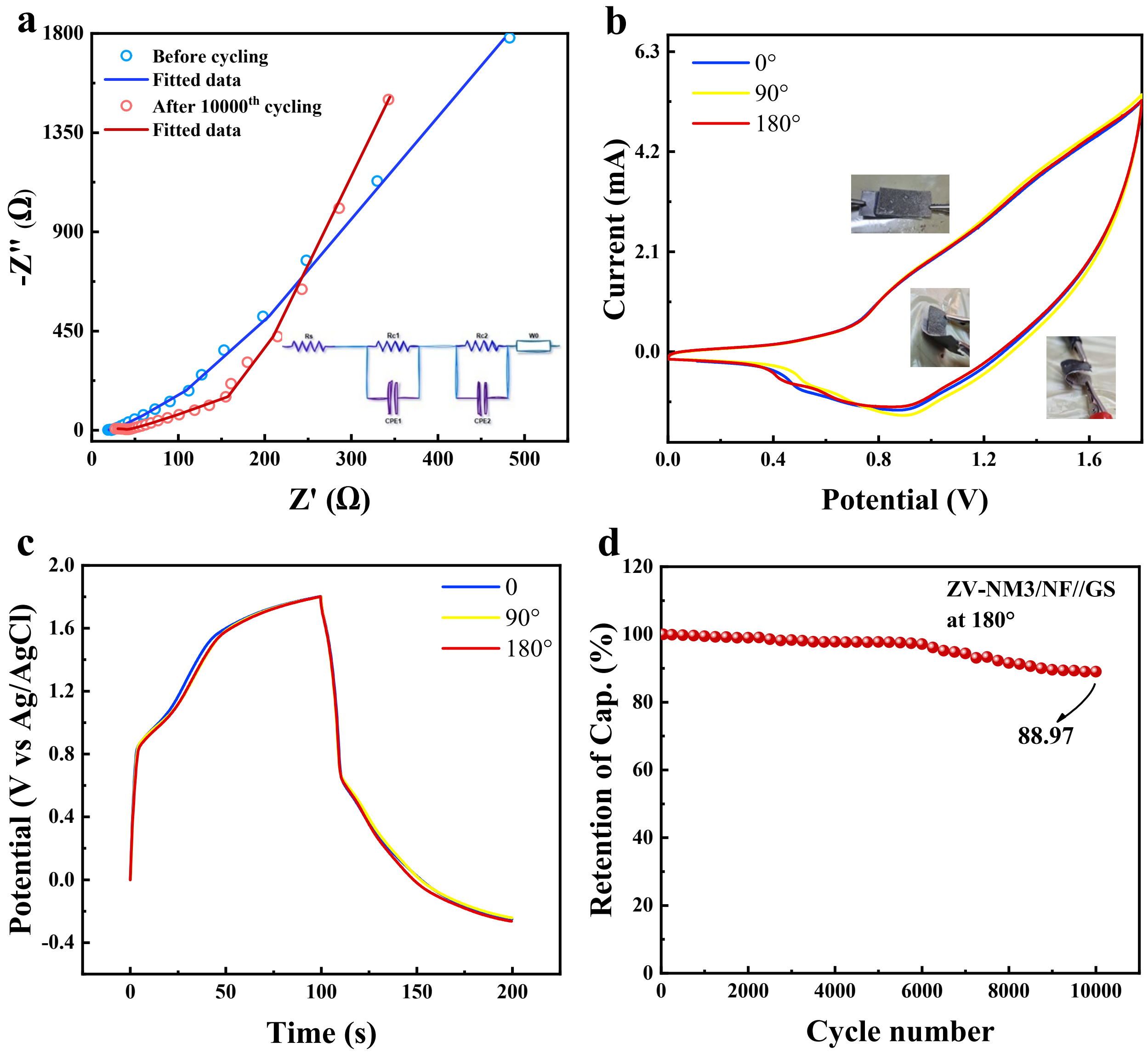

Figure S12: (a) EIS curves of before and after GCD cycles of ZV-NM3/NF//GS device, (b) CV curves at a scan rate of 20 mV s^{-1}, (c) GCD plots at 0.4 A g^{-1} in different bending states, and (d) Cycling stability at a current density of 8 A g^{-1} and a bending angle of 180˚ for the ZV-NM3/NF//GS device.

Table S5: The performance of all-solid-state ZV-NM3/NF//GS electrodes is compared with other recently reported flexible supercapacitors (Cs: Specific Capacitance, E_D: Energy Density, P_D: Power Density).

Reported Device	**Electrolyte**	**Cs**	**E_D (Wh kg^{-1})**	**P_D (W kg^{-1})**	**Cs retention (%) with cycles**	**Ref.**
$Ni_{0.5}Co_{0.5}MoO_4$//activated carbon	2 M KOH	53 C g^{-1}	16.2	725	5000 (80 %)	[9]
MNM-160//AC	2 M KOH	-	29.27	961.26	10000 (89.85 %)	[10]
$NiMoO_4$@CNT//AC	1 M KOH	210.51 C g^{-1}	32	2486	-	[11]
NMOS-2//AC	2 M KOH	60.8 F g^{-1}	21.62	800	10000 (85 %)	[12]
N–$NiMoO_4$@Ni_xB	2 M KOH	238 C g^{-1}	53.1	802	5000 (95 %)	[13]
$NiMoO_4$/C (D50)	3 M KOH	83 F g^{-1}	14.2	444	-	[14]
$NiMoO_4$@g-C_3N_4/RGO//AC	1 M Na_2SO_4	234.4 F g^{-1}	42.4	812	10000 (97 %)	[15]
$NiMoO_4$/MoO_3//AC	6 M KOH	99 F g^{-1}	33	1550	2000 (84.2 %)	[16]
FeOOH/c-$NiMoO_4$//AC	1 M KOH	115 F g^{-1}	40.8	800	2000 (94.2 %)	[17]
5%-Ce doped $NiMoO_4$	3 M KOH	210.2 F g^{-1}	29.2	833	10000 (80.55 %)	[18]
$NiMoO_4$/rGO-$_{450}$/PPy@NF	1 M KOH	218 F g^{-1}	43.65	600	-	[19]
$NiMoO_4$-2//AC	1 M KOH	115 F g^{-1}	35.9	2708	10000 (89.1 %)	[20]
ZV-NM3/NF//GS	**3 M KOH**	**110 F g^{-1}**	**45.4**	**1310**	**10000 (90.45 %)**	**This work**

Reference

1 M. Basak, M. L. Rahman, M. F. Ahmed, B. Biswas and N. Sharmin, *J. Alloys Compd.*, 2022, **895**, 162694.

2 B. Laïk, M. Richet, N. Emery, S. Bach, L. Perrière, Y. Cotrebil, V. Russier, I. Guillot and P. Dubot, *ACS Omega*, DOI:10.1021/ACSOMEGA.4C05082.

3 M. H. Azarian, S. Nijpanich, N. Chanlek and W. Sutapun, *RSC Adv.*, 2024, **14**, 14624–14639.

4 D. Liu, W. Zhang, H. Lin and N. Lin, *RSC Adv.*, 2025, **15**, 25940–25948.

5 L. Jing, K. Zhuo, L. Sun, N. Zhang, X. Su, Y. Chen, X. Hu, R. Feng and J. Wang, *J. Am. Chem. Soc.*, 2024, **146**, 14369–14385.

6 L. Q. Mai, A. Minhas-Khan, X. Tian, K. M. Hercule, Y. L. Zhao, X. Lin and X. Xu, *Nat. Commun.*, 2013, **4**, 1–7.

7 W. Sun, Y. Song, X. Q. Gong, L. M. Cao and J. Yang, *ACS Appl. Mater. Interfaces*, 2016, **8**, 820–826.

8 P. Siwatch, K. Sharma, N. Singh, N. Manyani and S. K. Tripathi, *Electrochim. Acta*, 2021, **381**, 138235.

9 S. Prabhu, M. Maruthapandi, A. Durairaj, S. Arun Kumar, J. H. T. Luong, R. Ramesh and A. Gedanken, *ACS Appl. Energy Mater.*, 2023, **6**, 1321–1331.

10 C. Koventhan and A. Y. Lo, *Chem. Eng. J.*, DOI:10.1016/j.cej.2024.149950.

11 S. Mumtaz, M. Alomar, A. Suman, M. Imran, A. Kumar, A. M. Afzal, Z. Chine, A. D. Oza, M. A. Diab and H. A. El-Sabban, *Inorg. Chem. Commun.*, 2025, **182**, 115255.

12 E. Li, L. Liu, L. Han, C. Guo, P. Liu and X. Liu, *J. Energy Storage*, 2025, **121**, 116605.

13 H. Che and A. Liu, *J. Colloid Interface Sci.*, 2025, **698**, 138066.

14 R. Yuvaraja, S. Sarathkumar, V. Gowsalya, S. P. Anitha Juliet, S. Veeralakshmi, S. Kalaiselvam, G. H. Gunasekar and S. Nehru, *Energy Adv.*, 2025, **4**, 94–105.

15 R. Hemalatha, K. Arunkumar, K. Karthik and D. M. Kalaiselvi, *J. Mater. Sci. Mater. Electron.*, 2025, **36**, 1–15.

16 M. P. Dabir, S. M. Masoudpanah and M. Mamizadeh, *J. Energy Storage*, 2024, **82**, 110542.

17 M. Huang, X. R. Shi, X. He, X. Zhang, F. Cao, P. Wang, C. Sun, S. Xu and M. Zhang, *Electrochim. Acta*, 2022, **427**, 140884.

18 A. Shameem, P. Devendran, A. Murugan, V. Siva, G. Ramadoss, H. Shamima and S. Asath Bahadur, *Sustain. Mater. Technol.*, 2023, **37**, e00661.

19 R. Ghanbari and S. R. Ghorbani, *J. Energy Storage*, 2023, **60**, 106670.

20 Q. He, X. Liu and X. Wu, *RSC Adv.*, 2024, **14**, 24749–24755.